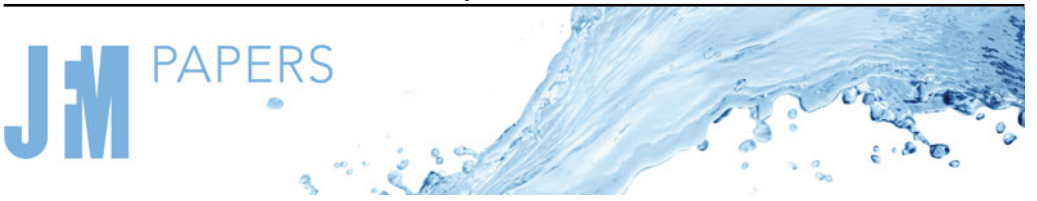
J. Fluid Mech. (2026), *vol.* 1029, A47, doi:10.1017/jfm.2026.11199



An experimental study investigating the inertial-wave field accompanying vortex rings translating through a rotating fluid

Oliver C. Jackson[1] **and Peter J. Thomas**[1]

[1]Fluid Dynamics Research Centre, School of Engineering, University of Warwick, Coventry CV4 7AL, UK

Corresponding author: Peter J. Thomas, p.j.thomas@warwick.ac.uk

(Received 4 September 2025; revised 10 December 2025; accepted 12 January 2026)

Results of an experimental study investigating issues of Coriolis effects on the fluid dynamics associated with vortex rings propagating through a rotating fluid are presented. The vortex rings are generated at the top of a large, water-filled rotating tank and they propagate downwards along the axis of rotation. The motion and the decay of the rings in a rotating fluid are expected to be accompanied by an inertial-wave field being established in the fluid surrounding the rings. However, the existence of this inertial-wave field had previously never been verified experimentally. Particle image velocimetry measurements were performed with the goal of demonstrating the existence of the inertial-wave field. Datasets were processed to extract individual inertial-wave modes and, for the first time, experimentally construct the dispersion relation for the inertial waves associated with vortex rings. For rotation rates when Coriolis forces dominate the dynamics, the experimental data are found to be in very good agreement with the well-established theoretical dispersion relation for inertial waves. The generation of inertial waves implies that kinetic energy is radiated away from the vortex rings. First results relating to the redistribution process of the kinetic energy are briefly discussed.

Key words: vortex dynamics, rotating flows, waves in rotating fluids

1. Introduction

Vortex rings represent a generic flow structure frequently studied to elucidate fundamental aspects of vortex dynamics. Early theoretical research on vortex rings dates back to, at least, the classic study by Helmholtz (1858). The first, detailed experimental investigation was performed by Kaden (1931). Studies on vortex rings propagating through a non-rotating fluid are abundant in the literature – for comprehensive overviews the reader

© The Author(s), 2026. Published by Cambridge University Press. This is an Open Access article, distributed under the terms of the Creative Commons Attribution licence (https://creativecommons.org/licenses/by/4.0/), which permits unrestricted re-use, distribution and reproduction, provided the original article is properly cited.

https://doi.org/10.1017/jfm.2026.11199 Published online by Cambridge University Press

is referred to, for instance, Shariff & Leonard (1992), Akhmetov (2009) and Danaila, Kaplanski & Sazhin (2021). However, investigations on vortex rings in a rotating fluid are very scarce.

The current study addresses aspects of the dynamics of vortex rings arising from Coriolis forces affecting vortex rings developing in a fluid that is subject to background rotation. The particular case considered here is that where the vortex rings concentrically enclose the axis of rotation of the system and propagate along the direction of that axis. As far as we are aware the only two existing experimental studies that have previously addressed this flow scenario are those by Verzicco *et al.* (1996) and Brend & Thomas (2009). One may expect vortex-ring motion in a rotating fluid to be accompanied by the generation of inertial waves within the ambient bulk fluid. The results presented here focus on the inertial-wave field surrounding such vortex rings propagating and decaying subject to background system rotation.

Inertial waves are a particular type of mechanical wave that can be generated in rotating fluids (cf. Davidson 2013). Inertial waves are internal waves. That is, they propagate within the fluid rather than at its surface. Inertial waves arise as a consequence of the Coriolis force representing a restoring force that tries to return displaced fluid to its equilibrium position. The Coriolis force (per unit volume) is given by

$$F_C = -2\rho\, \boldsymbol{\Omega} \times \boldsymbol{u}, \tag{1.1}$$

where ρ is the density of the fluid, $\boldsymbol{\Omega}$ is the angular velocity vector and $\boldsymbol{u}$ is the velocity vector. As a consequence of the cross-product in (1.1) the Coriolis force always acts at a right angle to the direction of motion and that is the reason for it acting as a restoring force. The cross-product also leads to the peculiar characteristic that the phase velocity of inertial waves is perpendicular to their group velocity, the latter being a measure of the rate and direction of energy transfer. The dispersion equation for inertial waves is given by

$$\omega = \pm 2\Omega \cos\theta = \pm 2\Omega \frac{\boldsymbol{k} \cdot \boldsymbol{\Omega}}{k\Omega}, \tag{1.2}$$

where $\boldsymbol{k}$ is the wave vector and θ is the angle between the axis of rotation and the direction of the particular wave mode (see figure 1). Thus, any particular direction θ of wave motion is associated with an inertial wave with a unique frequency ω. In particular, since $|\cos\theta| \leq 1$, the highest possible inertial-wave frequency is 2Ω and for this mode the wave vector, $\boldsymbol{k}$, is aligned with the rotational axis.

The only existing study addressing the issue of inertial waves in connection with vortex rings propagating along the axis of rotation in a rotating fluid was performed by Verzicco *et al.* (1996). They conducted a combined experimental and computational programme. Key results of their investigations were that moderate levels of background rotation lead to a decrease of the translation velocity of the rings. Concurrently a structure with opposite circulation was observed to form ahead of the ring, accompanied by the generation of an intense axial vortex on the axis of symmetry in the tail of the ring. They moreover observed that, when rotation rate is sufficiently high for the motion to be dominated by Coriolis forces, then vortex rings hardly formed. Subsequently Brend & Thomas (2009) performed experiments complementing those of Verzicco *et al.* (1996). They determined an estimate for the decay length that vortex rings can travel along the axis of rotation for successively increasing rotation rates. That is, the distance that rings can travel until they have fully lost their structural integrity. In the context of their study, Brend & Thomas (2009) also briefly addressed the flow structure ahead of the vortex rings and in their wake, when the rings are subject to background rotation.

https://doi.org/10.1017/jfm.2026.11199 Published online by Cambridge University Press

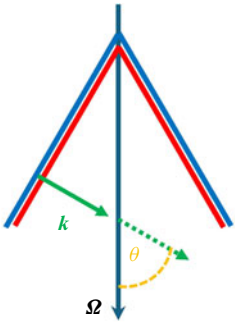


Figure 1. Definition of angle θ. The angular velocity vector, $\boldsymbol{\Omega}$, is displayed as pointing downwards because the turntable, together with the experimental equipment to be described in § 2, rotates in a clockwise sense when viewed from above. The simplified sketch is for illustrative purposes of the angle θ solely. It does not account for other details of the wave field.

The experimental particle image velocimetry (PIV) data of Verzicco *et al.* (1996) were not sufficient to yield experimental evidence of the presence of inertial waves in the flow field surrounding the vortex rings. However, together with their experimental data they discuss computational simulations and identify contours of azimuthal vorticity about which they write that 'it is tempting to identify these structures as inertial waves which allow the ring to radiate energy' (Verzicco *et al.* 1996, p. 233, lines 3–4).

Based on the results of Taylor (1922), Verzicco *et al.* (1996), Scase & Terry (2018) and Crowe, Kemp & Johnson (2021), the existence of inertial waves surrounding the vortex rings has to be expected – of course. The contours of azimuthal vorticity for vortex rings in Verzicco *et al.* (1996) are visually similar to the theoretical streamline contours by Taylor (1922) who considered inertial waves for the related case of a rigid sphere propagating through a rotating fluid along the axis of rotation. Similarly, the theoretical analyses of Scase & Terry (2018) and Crowe *et al.* (2021) indicated an inertial-wave field surrounding Hill's spherical vortex in a rotating fluid moving along the axis of rotation.

Nevertheless, a definitive experimental confirmation of the existence of the inertial-wave field in the liquid ambient to the vortex rings requires experimental data suitable for a direct comparison with the theoretical dispersion curve of (1.2). However, at the time of the study of Verzicco *et al.* (1996), over thirty years ago, the experimental PIV methodology and the required image processing procedures, requiring the collection and analysis of very large digital datasets, were not advanced enough to isolate individual inertial-wave frequency modes in the flow field together with their associated propagation angles with respect to the axis of rotation (cf. Verzicco *et al.* 1996, p. 234, lines 3–5). Thus, it was not possible for Verzicco *et al.* (1996) to produce experimental data revealing clear evidence of the presence of inertial waves. Therefore, it was also impossible to produce experimental data enabling a direct comparison with the theoretical dispersion equation (1.2). That is, experimental data revealing how the frequency of individual inertial-wave modes relates to their associated propagation angle. Thus, the purpose of the current study was to use modern, state-of-the-art data collection and image and data processing methodologies to close that gap.

2. Experimental set-up

The experiments summarised here were conducted using Warwick's large rotating-tank facility. The rig is schematically illustrated in figure 2(*a*). The facility constitutes a

https://doi.org/10.1017/jfm.2026.11199 Published online by Cambridge University Press

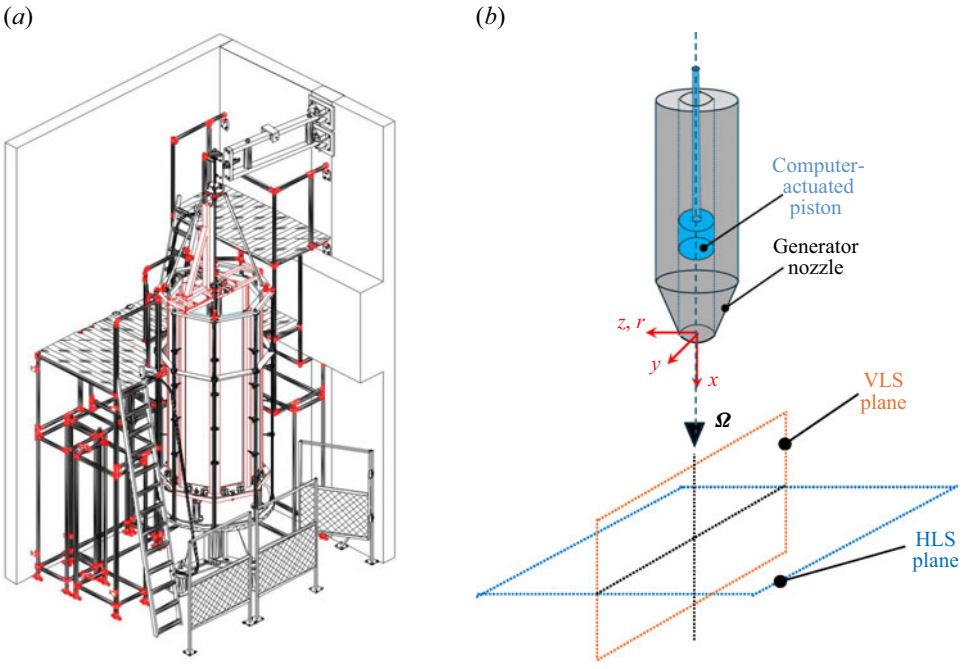


Figure 2. Experimental facility. (*a*) Illustration of the large-scale rotating-tank facility at the University of Warwick. The overall height of the facility is over 5.7 m, the height of the water tank on the turntable is 2.5 m and the across width of the octagonal tank is 1.0 m. (*b*) The vortex-generator nozzle–piston arrangement with coordinate system and illustration of vertical (VLS) and horizontal (HLS) planes of the PIV light-sheet orientation. The exit radius of the vortex-generator nozzle is $r_0 = 25$ mm. A video showing the facility rotating is available as supplementary movie 1.

tank of height 2.5 m, with octagonal cross-section and across width of 1 m, which is mounted on top of a rotating turntable. The overall height of the facility, from the floor to the top of the support structure, is over 5.7 m. The main features of the rig are outlined below and detailed descriptions of all components can be found in Jackson (2025). The facility in rotation is shown in supplementary movie 1 available at https://doi.org/10.1017/jfm.2026.11199.

The turntable is driven by a 7.5 kW Siemens M132M4 electric motor producing 511 N m torque. The motor is connected to a gear box and rotates the rig via a belt drive. The speed of the turntable is controlled by an analogue potentiometer, and the speed is monitored by a digital rotation-speed sensor.

The vortex rings were generated using a piston-type generator nozzle whereby a computer-controlled piston ejects water from a nozzle with circular cross-section. The arrangement is illustrated in figure 2(*b*). The sense of rotation of the turntable is clockwise when viewing downwards from above. To correctly reflect this physical configuration, the vector $\boldsymbol{\Omega}$ points downwards in figures 1 and 2(*b*). The piston is driven by a Parker ER Series actuator which transforms the rotary movement of an associated stepper-motor into linear motion. The system is configured to yield 1000-step revolution of the motor over 100 mm linear motion, providing an accuracy of ± 0.1 mm for the positioning of the piston. The exit radius of the generator nozzle is $r_0 = 25$ mm. The generator nozzle is rigidly mounted at the top of the rotating tank. The centre of the exit nozzle is aligned to coincide with the rotational axis of the turntable. The vortex rings were released vertically downwards from the generator nozzle submerged in the water inside the tank. It

https://doi.org/10.1017/jfm.2026.11199 Published online by Cambridge University Press

is emphasised that the nozzle rotates with the tank. Thus, during ejection of water from the nozzle there exists no pre-enforced shear between the discharged fluid and the ambient fluid.

Vortex rings were generated for piston speeds $U_P \leq 200\,\mathrm{mm\,s^{-1}}$, piston strokes $L_P \leq 100\,\mathrm{mm}$ and a maximum rotation rate of the tank of 12 rpm, corresponding to maximum rotational velocities of $\Omega \leq 1.26\,\mathrm{rad\,s^{-1}}$ and associated rotational frequencies of the turntable of $F_\Omega = \omega/2\pi$.

The Rossby number is defined as

$$Ro = \frac{U_P}{2\Omega L_P}\,. \tag{2.1}$$

Following Glezer (1988), the Reynolds number is defined as

$$Re = \frac{U_P L_P}{\nu}\,, \tag{2.2}$$

with a kinematic viscosity of water $\nu = 1\,\mathrm{mm^2\,s^{-1}}$. Note that using the piston stroke L_P in (2.1) and (2.2) also ensures that the information about the ejected liquid volume is captured. If required, the L_P-based definitions of the Rossby and Reynolds numbers can be translated into corresponding diameter-based values by simple geometric considerations for future experiments that may use other nozzle diameters. For the current experiments we only had access to the single nozzle with radius $r_0 = 25\,\mathrm{mm}$. It was not feasible to vary the nozzle diameter because manufacturing and fitting nozzles with different diameters requires substantial technical workshop resources. For the existing nozzle, experiments were conducted for a minimum Rossby number of $Ro = 0.8$ and Reynolds numbers in the range $1250 \leq Re \leq 10\,000$. Note that the maximum rotation rate of 12 rpm ensures that, with reference to the results of Brend & Thomas (2009), the vortex rings disintegrate within a distance of less than one nozzle diameter from the generator nozzle.

In preparation for the experiments, the water inside the tank was allowed to adjust to the rotational speed of the turntable, after the table had been accelerated to the desired rotation rate. This ensured that the liquid was in a state of solid-body rotation when the experiments commenced. This adjustment process required up to 6 h for the lowest rotation rates used.

Following the ejection of each vortex ring it was required for the residual motion inside the tank to subside and let the system readjust to solid-body rotation before the next vortex-ring generation could be initiated. For high rotation rates it was found that the time required for this process to be completed was of the order of 10 min. However, for a stationary tank and lowest rotation rates it required as long as an hour.

The laboratory in which the turntable facility is housed is fully air conditioned. Moreover, there exist a number of additional fans distributed throughout the laboratory facilitating agitation and mixing of the ambient air in the laboratory. This ensures that the possibility of vertical temperature gradients developing over long time periods within the liquid inside the tank is minimised. The temperature of the laboratory was kept at 20 °C, implying a water density of $\rho_w = 0.9982\,\mathrm{g\,cm^{-3}}$.

Flow-field measurements were performed by means of PIV. The entire PIV systems was mounted on the rotating turntable, that is, within the rotating frame of reference. The PIV system utilised a 4 W continuous laser with a wavelength of 532 nm. The light sheet produced had a thickness of 2 mm. The seeding particles used for the PIV experiments were Plascoat 'Talisman 30' polymer powder with a mean particle diameter of $d_p = 150\,\mu\mathrm{m}$ and a density of $\rho_p = 0.99\,\mathrm{g\,cm^{-3}}$ – as specified by the manufacturer. The Talisman particles are normally used for plastic coating of metals. The density difference of circa 0.2 % between the particle density and the water density implies a

https://doi.org/10.1017/jfm.2026.11199 Published online by Cambridge University Press

(upwards) settling velocity of the particles of $v_s = (\rho_p - \rho_w)gd_p^2/\mu = 1.8 \times 10^{-5}\,\mathrm{m\,s^{-1}}$. It was observed, however, that some particles rose to the water surface while others sunk to the bottom of the tank, implying a distribution of the particle density around the manufacturer-specified value for ρ_p.

The PIV video frames were acquired using FLIR Blackly S USB3 cameras with Sony IMX392 image sensors. These $1/2.3''$ CMOS sensors allow for 12-bit colour recordings at rates up to 165 frames per second. The image resolution is $m = 1200$ rows of pixels and $n = 1920$ columns of pixels, in landscape orientation. The cameras were configured with a software trigger for frame capture. This enabled full synchronisation of the camera with the vortex-ring piston-control system using a custom Python script. The PIV video recordings were processed using the open-source PIVlab software described in Thielicke and Stammhuis (2014) and Thielicke & Sonntag (2021). The PIV interrogation window for all reported data was 16 pixels $\times$16 pixels with a 50 % overlap, for which PIVlab generated $149 \times 239 = 35\,611$ velocity-data points per video frame. As part of the data analysis to follow, individual velocity-data points will be referred to by p, q, with $1 \leq p \leq 149$ and $1 \leq q \leq 239$, and where p identifies the data-point row and q the data-point column. For further details such as PIV calibration, pre-processing and post-processing of the PIV data, filtering methods for the recordings for noise reduction and increasing image sharpness, data analysis procedures, etc., the reader is referred to Chapter 5 of Jackson (2025, pp. 48–84). That chapter presents a detailed error analysis enabling the evaluation of the run-to-run variations involved in the experiments conducted. It reveals that the run-to-run variations are very small.

Experiments were conducted with the PIV light sheet alternatively aligned horizontally (HLS) or vertically (VLS) as illustrated in figure 2(*b*). That is, for the HLS mode the axis of rotation of the system was perpendicular to the light sheet. For the VLS mode the light sheet was adjusted such that the axis of rotation of the system lay within the plane of the light sheet. The frame rates for the recordings varied in the range 60−150 frames per second, depending on the particular measurements performed at any time.

For each set of experimental conditions, the data from ten runs of the experiment were averaged. The overall data presented are based on the analysis of PIV recordings of a total of around 600 vortex rings. Each ring yielded approximately 8−9 GB of data. The total amount of PIV data captured for the results summarised here were around $600 \times 9\,\mathrm{GB} = 5.4\,\mathrm{TB}$. The analysis of the data for each ring required about one hour on 42 CPU threads, corresponding to $600 \times 42 = 25\,200$ core hours.

For further details relating to the vortex-ring facility at the University of Warwick and details underlying the technical specifications of all components associated with the rig, the reader is referred to Jackson (2025).

3. Results

3.1. *Streamline patterns*

Figure 3 displays streamline patterns obtained from the data analysis conducted by means of PIVlab. The streamline patterns have been superposed onto a photograph of the vortex-generator nozzle that can be seen in the background, at the top of the images. In each of figures 3(*a*)–3(*c*) the displayed streamfunctions are separated from one another by equidistant streamfunction values. However, the separation interval varies between the three figures. The values used were selected to enable a clear, qualitative evaluation of the flow field. Figures 3(*a*)–3(*c*) represent rings with Rossby numbers of, respectively, $Ro = \infty$, 1.6 and 0.8, corresponding to rotation rates of 0, 6 and 12 rpm, at a Reynolds

https://doi.org/10.1017/jfm.2026.11199 Published online by Cambridge University Press

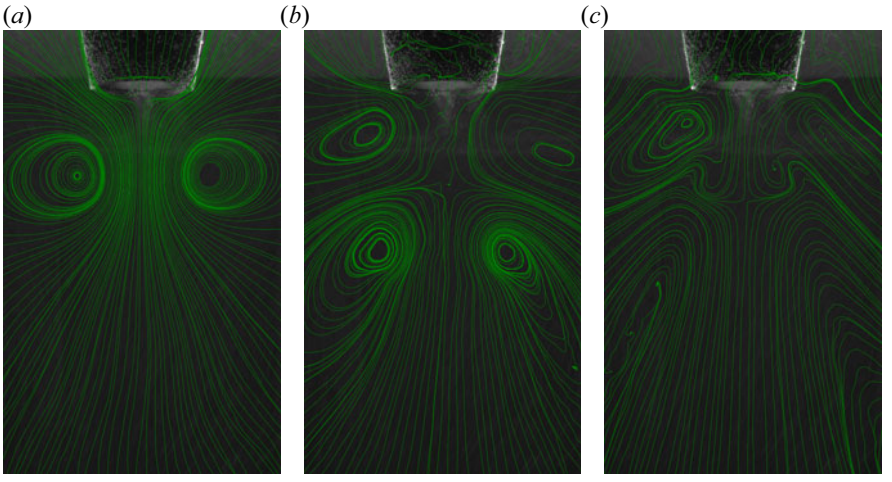


Figure 3. Streamline pattern superposed onto an image of the generator nozzle for vortex rings generated with piston stroke $L_p = 100\,\text{mm}$, piston velocity $U_p = 100\,\text{mm}\,\text{s}^{-1}$, i.e. $Re = 5000$, and (*a*) a non-rotating system $Ro = \infty$ (0 rpm), (*b*) at $Ro = 1.6$ (6 rpm), and (*c*) at $Ro = 0.8$ (12 rpm). The field of view displayed in the figures extends vertically to $x/r_0 \approx 7.5$, and horizontally across the image over the interval $-2.6 \lessapprox r/r_0 \lessapprox 2.6$. Associated animations can be found as supplementary movies 2–4.

number $Re = 5000$. The static images in figure 3 cannot properly convey the complexity of the streamline patterns, their changes and dynamics as the Rossby number decreases. Therefore, the animations associated with the three images can be found as supplementary movies 2–4. The observations and the data analysis have revealed that the flow field remains reasonably axisymmetric until the rings break down. Upon this the flow field becomes turbulent in that region. However, the far field was observed to largely maintain its axisymmetry.

Figure 3 and the associated animations qualitatively illustrate the fundamental changes of the flow-field pattern as the Rossby number decreases and Coriolis begin to dominate the dynamics. Figure 3(*a*) shows the typical streamline pattern associated with vortex rings in a non-rotating system, as previously displayed in similar form in the published literature. However, for the case of rings in the rotating system, at $Ro = 1.6$ and 0.8 one can identify changes of the streamline patterns mirroring the contour lines of the computational results in figures 14–16 of Verzicco *et al.* (1996).

The streamline patterns in figures 3(*b*) and 3(*c*) provide clear experimental evidence of the effects of increasing background system rotation on the flow dynamics. The nature of the streamline patterns in these two figures does also somewhat resemble the theoretical streamline patterns for spherical vortices displayed in figures 2 and 4 of Taylor (1922) and figures 1–3 of Scase & Terry (2018). In the context of the discussion provided in Taylor (1922) and Scase & Terry (2018), the streamline patterns in figures 3(*b*) and 3(*c*) therefore almost certainly reflect the presence of inertial waves. Note, however, that the streamline patterns in figures 3(*b*) and 3(*c*) are associated with a superposition of all inertial-wave modes present in the wave field. In § 3.2 the velocity data discussed are filtered to enable extracting individual inertial-wave modes with different frequencies and with different propagation directions. Note also that the structures that appear to be secondary vortex rings in figures 3(*b*) and 3(*c*), located between the actual vortex ring and the nozzle exit, are not vortex rings. To appreciate this, see supplementary movies 2–4. These videos reveal that the structures that appear to be secondary vortex rings in the stills can shortly later be seen to represent the roots of inertial waves. The vortex ring is easily identified in the

https://doi.org/10.1017/jfm.2026.11199 Published online by Cambridge University Press

non-rotating case in the still image in figure 3(*a*). However, for the rotating cases it is recommended to view the supplementary movies to clearly identify it.

3.2. *Visualisation of inertial waves*

As outlined in § 1 the overriding goal of the study was to confirm the existence of the inertial-wave field in the flow region surrounding the vortex ring by isolating different frequencies through appropriate filtering of the PIV data of the VLS plane and thereby becoming able to experimentally reproduce the dispersion relation given by (1.2). Samples of visualisations of inertial waves will be displayed. This is done separately for the PIV data sampled in the VLS and the HLS planes identified in figure 2(*b*). For both the VLS and the HLS data, it is demonstrated that the inertial waves can be identified independently in each of the two velocity components associated with the two perpendicular PIV data-sampling modes. In § 3.4.2 the filtered VLS data are used to demonstrate that the data follow the theoretical dispersion curve of (1.2).

3.2.1. *Data processing to isolate inertial-wave modes from PIV data of VLS plane*

The dispersion curves for the inertial waves can only be reconstructed from experimental PIV velocity data obtained in the VLS plane of figure 2(*b*). That is because, according to (1.2), the different inertial-wave modes of frequencies ω rely on the angle θ between the axis of rotation and the direction of the particular wave mode.

Thus, the inertial waves are associated with velocity components u and v in the directions of, respectively, the x and y coordinate axes in figure 2(*b*). The PIV data for the velocity components u and v were analysed separately to demonstrate that the theoretical dispersion curves can be reconstructed experimentally from both velocity components independently. The data-analysis process is briefly outlined by referring to the velocity component u, on the understanding that the velocity component v was independently subjected to the corresponding process.

In order to extract the different wave modes, it is required that the PIV velocity data are filtered for the particular mode that is to be identified. The data analysis proceeded successively for all of the $p \times q = 149 \times 239$ velocity-data points for sequences of video recordings. In preparation for the filtering process the mean-flow component $\overline{u}(p, q)$, averaged over all velocity-data points p, q and all video frames, was initially calculated. That mean value was subtracted from the PIV data $u(p, q, t)$ for each velocity-data point to isolate the fluctuating component $u'(p, q, t) = u_(p, q, t) - \overline{u}(p, q)$ associated with point p, q. However, it is noted that removing $\overline{u}(p, q)$ had very little effect on the final data since it was two orders of magnitude smaller than $u_(p, q, t)$.

The fluctuating component $u'(p, q, t)$ is then subjected to a Fourier transform $\hat{f}$ defined by

$$\hat{f}\left(u'(p, q, t)\right) = \int_{-\infty}^{+\infty} u'(p, q, t)\, \mathrm{e}^{-\mathrm{i}\omega t}\, \mathrm{d}t = F_{p,q}\left(\frac{\omega}{2\pi}\right) . \tag{3.1}$$

Since the experimental data are not a continuous function a discrete Fourier transformation is computed using a fast Fourier transform (FFT) algorithm. The frame rate of 60 Hz of the PIV recordings implies a Nyquist frequency of 30 Hz. This is substantially above the expected maximum frequency of the inertial waves – for the current study $f_{max} = (1/2\pi)\, \omega = (1/2\pi)\, 2\Omega = (1/\pi) \times 1.26$ rad s$^{-1} \approx 0.40$ Hz.

The number of samples determines the number of frequency bins that the fast Fourier transform can allocate. The number of frequency bins represented the largest issue associated with the data analysis. The maximum frequency of the inertial waves is $\omega = 2\Omega$

https://doi.org/10.1017/jfm.2026.11199 Published online by Cambridge University Press

and the number of frequency bins within this range depends on the rotation rate of the rotating turntable. For instance, a rotation rate of 12 rpm corresponds to a rotational velocity of $2\pi \times 12\,\text{rpm}/60\,\text{s} = 2\pi/5\,\text{rad s}^{-1}$. This corresponds to a rotational frequency of 1/5 Hz, such that the maximum inertial-wave frequency is $2 \times 1/5$ Hz. For a recording of length 60 s, at a recording rate of 60 frames per second, there are 3600 samples. Thus, the number of frequency bins is 1800 while the Nyquist frequency is 30 Hz. Consequently, the width of each bin is $30\,\text{Hz}/1800 = 1/60$ Hz. Therefore, the number of bins in the inertial-wave range is $(2/5)\,\text{Hz}/(1/60)\text{Hz} = 24$ bins. Since the maximum inertial-wave frequency decreases linearly with the rotational frequency of the rotating tank so does the number of bins. That implies very low numbers of bins at lowest rotation rates. Increasing the recording length to increase the number of samples, and therewith the number of bins, cannot resolve the issue. That is, because the vortex rings decay, and due to viscous dissipation, the strength of the signals decay. Thus, the issue outlined above represents a natural limit associated with identifying inertial waves associated with the motion of vortex rings in a system subject to background rotation. Nevertheless, the data to be presented display good agreement with the theoretical dispersion curve for the highest rotation rates used and where vortex rings still existed for sufficiently long as a coherent structure before disintegrating due to the destabilising effects (cf. Brend & Thomas 2009) of the background rotation.

Once the velocity field has been passed into the Fourier domain, band filters were applied according to the upper and lower limits of the frequency bins where, for each bin, ω_H identifies the centre frequency of the bin. Spectrum frequencies within each bin, around ω_H, were mildly attenuated using a Hann window. The filtered data were then transformed back into the time domain according to (3.2):

$$u'_H(p,q,t) = \hat{f}^{-1}\left(F_{p,q}(\omega_H)\right) = \frac{1}{2\pi}\int_{-\infty}^{+\infty} F_{p,q}(\omega_H)\,\mathrm{e}^{\mathrm{i}\omega t}\,\mathrm{d}\omega\,, \tag{3.2}$$

with associated values $F_f = \omega_H/2\pi$ for the filtered frequency.

3.2.2. *Inertial wave modes in VLS plane*

Figures 4 and 5 display typical examples of visualisations of inertial-wave modes obtained by the single-frequency filtering described in § 3.2.1. The particular waves shown are those corresponding to propagation angles of $\theta = 65°$, 45° and 25°. Figure 4 displays results obtained from processing the data for the axial flow component, in the x direction of the coordinate system in figure 2(*b*), while figure 5 shows the corresponding results obtained from processing the radial flow component. The results of the analysis for both individual components are included to highlight that it is possible to extract individual Fourier modes from each of the two velocity components independently. The red and blue line patterns radiating away from the area of the nozzle, located at the top of each figure, represent the phases of the inertial waves. The figures reveal that the inertial-wave modes associated with the particular θ directions are very clearly visible, in analogous form, as red and blue bands for the data from both velocity components. Sample animations illustrating the motion of the wave modes, in real-time speed, for different filtering frequencies are available as supplementary movies 5–7.

The inertial waves are visible all the way to the central axis axis of the tank. This is due to the removal of the mean flow velocity $\overline{u}_{m,n}$ from the signals $u_{p,q}(t)$. The procedure effectively removes the influence of the vortex ring itself from the flow. While the filtering also eliminates the mean, the underlying idea was to centre the fluctuations around zero. Nevertheless, quantitatively, the results appeared to filter more effectively when the mean

https://doi.org/10.1017/jfm.2026.11199 Published online by Cambridge University Press

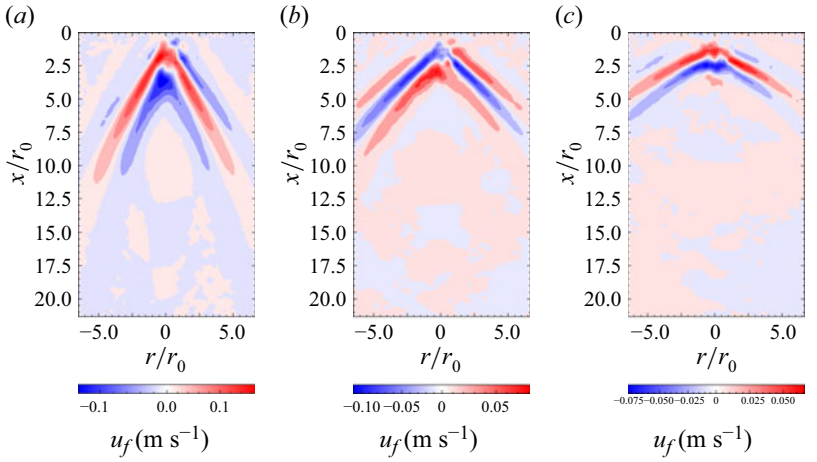


Figure 4. Instantaneous filtered axial velocity contours at $Ro = 1.6$ (12 rpm), where the frequency filtered for corresponds to the direction (*a*) 65°, (*b*) 45°, and (*c*) 25°. Typical illustrative animations are available as supplementary movies 5–7.

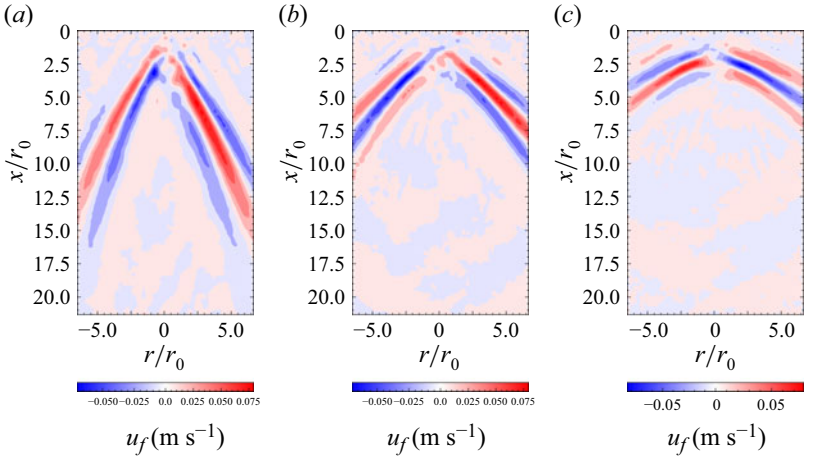


Figure 5. Instantaneous filtered radial velocity contours at $Ro = 1.6$ (12 rpm), where the frequency filtered for corresponds to the direction (*a*) 65°, (*b*) 45°, and (*c*) 25°.

was subtracted from the flow. To inspect images of the mean flow, the reader is referred to Jackson (2025, figures 6.14 and 6.15, pp. 109–110).

The extent of the inertial waves is of interest as they extend significantly further down the axis of the tank than the vortex ring itself propagates at the highest rotation rates, where the rings disintegrate close to the nozzle exit. For the higher filtering angles one can also identify reflections of the inertial waves from the wall of the tank. These are the faint, light-blue band structures visible further down in the tank, for $x/r_0 \lesssim 12$, in some of the subplots in figures 4 and 5 and which represent areas of constructive interference. One of these structures is, for instance, the light-blue band originating in figure 5(*b*) near $r/r_0 \approx -6.5$, in the interval $12.5 \lesssim x/r_0 \lesssim 15.5$, and running downwards from there towards the axis of rotation.

https://doi.org/10.1017/jfm.2026.11199 Published online by Cambridge University Press

3.3. *Inertial waves in HLS plane*

When collecting PIV data in the HLS plane (see figure 2*b*) the associated velocity components are the v and the w component in, respectively, the y and the z coordinate directions. It is these components one obtains from the data analysis in PIVlab from image frames with square pixel and data-point arrangements. However, for the data representation it is more convenient and useful to work in polar coordinates r, ϕ. Therefore, the v and w velocity components were transformed into velocity components u_r and u_ϕ in the $y{-}z$ plane. Here ϕ is the polar angle between locations in the HLS light sheet of figure 2(*b*) around the x-coordinate direction. Due to the underlying symmetry of the flow geometry at the nozzle exit in figure 2(*b*) the radial velocity u_r can be assumed to correspond to the velocity component v for the VLS data in § 3.2.2. Of course some deviations from the symmetry can naturally develop as the rings propagate downwards, away from the nozzle exit.

However, the idealised geometric symmetry defining the problem implies that the individual inertial-wave modes of figures 4 and 5 have to be imagined as cones of opening angle θ, where the x axis represents the vertical centreline of the cones. Thus, when viewed in the HLS plane one expects to see the inertial waves represented as concentric circles. This is schematically illustrated in the sketch in figure 6(*a*). Moreover, when a ring approaches the HLS plane, one expects to see the circular, concentric representations of the inertial-wave modes moving towards the x axis in the processed data as the apex of the inertial-wave cone moves towards the HLS plane. If the vortex ring has not disintegrated before passing through the HLS plane the waves should be seen as moving outwards.

Identifying the angle θ directly, by means of the methodology summarised in § 3.2.1, is relatively straightforward. The angle could be obtained indirectly from data measured in the HLS plane by analysing the radial phase velocity of the waves. However, such methodology was not implemented as part of our study. Thus, the inertial waves displayed in this section only constitute visualisations of the superposition of all inertial-wave modes. Figures 6 and 7 display, respectively, the velocity components u_r and u_ϕ obtained from the measurements in the HLS plane for vortex rings generated with Reynolds numbers $Re = 5000$ and Rossby numbers $Ro = \infty,\ 4.77$ and 0.8. A typical, illustrative animation showing the wave motion in the HLS plane, at $Ro = 0.8$, is available as supplementary movie 8. At this low Rossby number the ring decayed before passing through the HLS plane. One sees circular wave fronts moving radially inwards. This is consistent with the supplementary movies referred to in the caption of figure 4. There the motion is in the direction of the wave vector, towards the axis of rotation. Near the end of the animation in supplementary movie 8 the waves are beginning to slowly fade away, due to dissipation. At higher Rossby numbers the waves appeared increasingly fainter as is illustrated by the images in figures 6 and 7.

In figure 6 the image for the ring at $Ro = \infty$ (0 rpm) at the instant $t = 5$ s (top-left corner) shows a single red, circular structure in the centre of the image. This structure can obviously not be associated with inertial waves since the system is not rotating. What the structure represents is the outward-directed radial velocity at the front of the vortex ring as it approaches the HLS plane from above. At $t = 7$ s one sees a blue ring in the centre of the image. This represents the inward-directed radial velocity after the ring has fully propagated across the HLS plane. At $t = 15$ s the ring is sufficiently far below the HLS plane such that the PIV system can no longer detect any significant flow motion. At low rotation rates, corresponding to $Ro = 4.77$, the situation for u_r essentially still mirrors that for the case of $Ro = \infty$ at $t = 7$ s. That is, at $Ro = 4.77$ the background rotation has not yet led to significant effects on the radial flow component. It is seen in figure 7 that the

https://doi.org/10.1017/jfm.2026.11199 Published online by Cambridge University Press

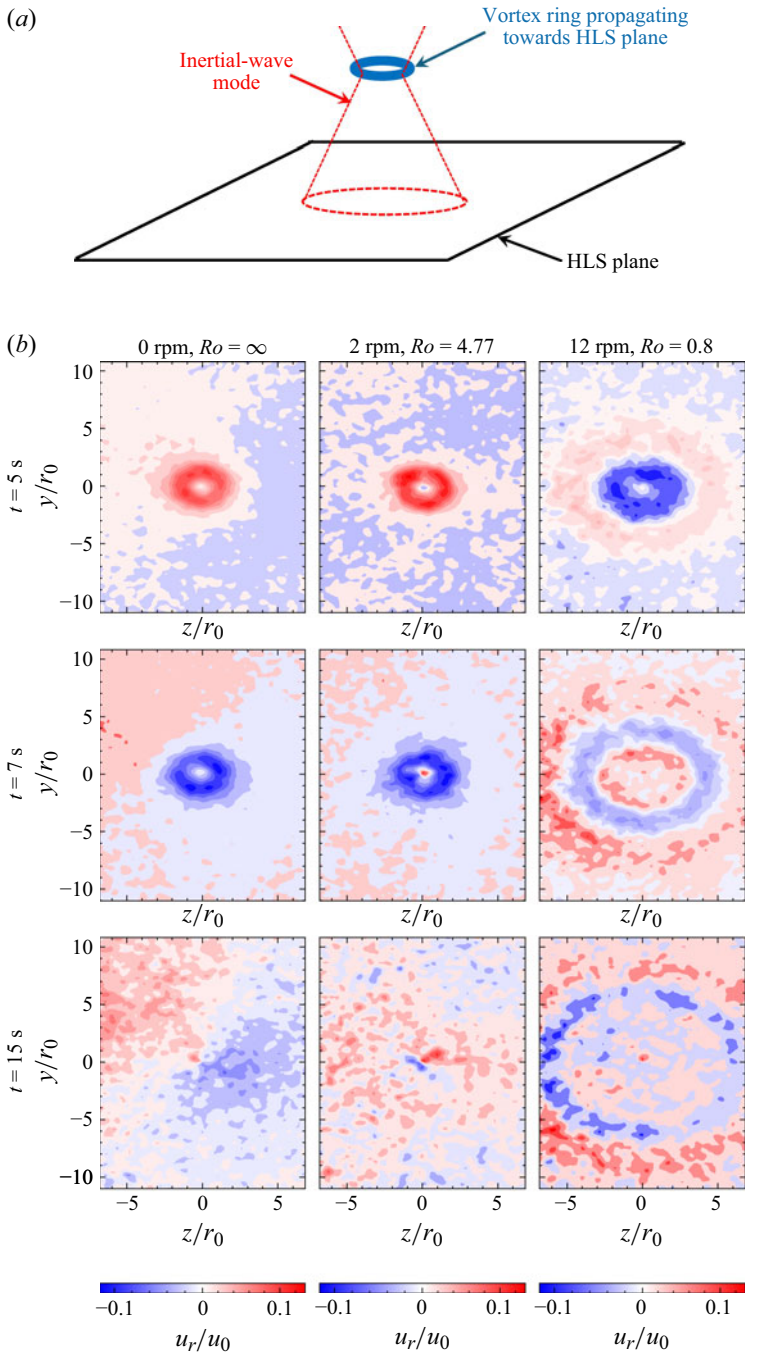


Figure 6. (*a*) Vortex ring emitting conical inertial waves while approaching the HLS light-sheet plane. (*b*) Distribution of radial velocity u_r at different times and for Rossby numbers, measured using an HLS plane PIV light sheet, $Re = 5000$. Top row, $t = 5$ s; middle row, $t = 7$ s; bottom row, $t = 15$ s; left column, $Ro = \infty$ (0 rpm); middle column, $Ro = 4.77$ (2 rpm); right column, $Ro = 0.8$ (12 rpm). Typical, illustrative animation for $Ro = 0.8$ is available as supplementary movie 8.

https://doi.org/10.1017/jfm.2026.11199 Published online by Cambridge University Press

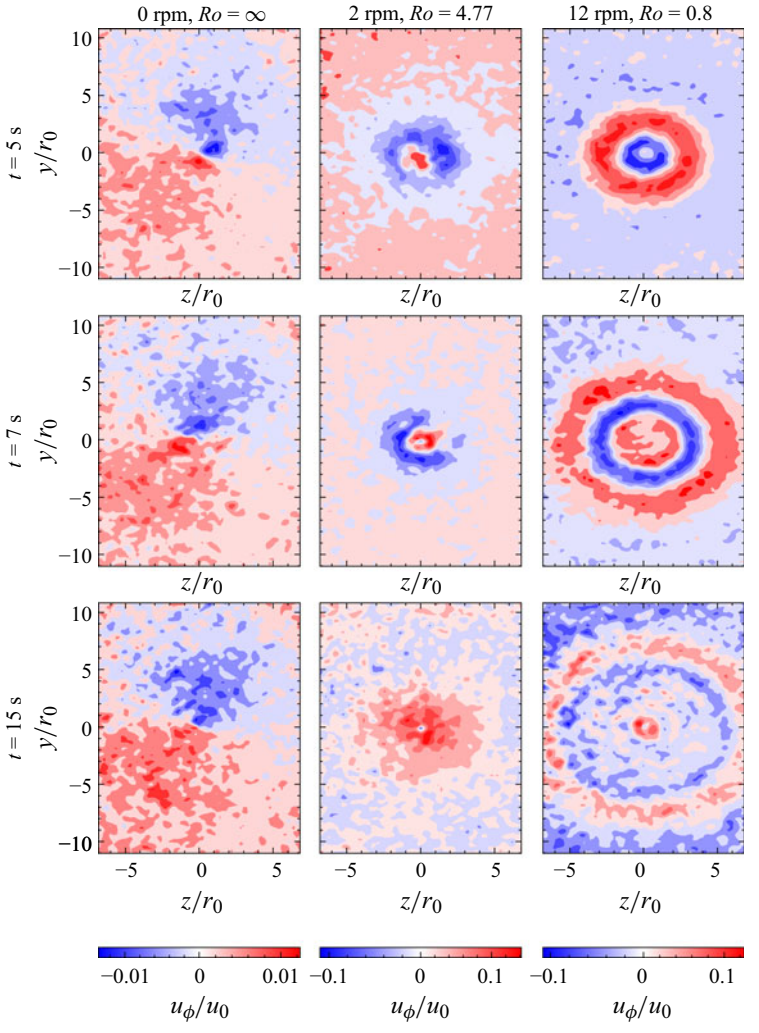


Figure 7. Distribution of the azimuthal velocity u_ϕ at different times $t = 5$, 7, 15 s, measured using a PIV light sheet in the HLS plane at $Re = 5000$ for $Ro = \infty$ (0 rpm), $Ro = 4.77$ (2 rpm) and $Ro = 0.8$ (12 rpm). Typical, illustrative animation is available as supplementary movie 8.

situation is different in the case for the azimuthal flow velocity u_ϕ. For the lowest Rossby number of $Ro = 0.8$, the right-hand column of plots in figure 6, one can clearly identify the signature of inertial waves as concentric red and blue circles. One can further see that the location of the circles in the figures has changed between $t = 7$ s and $t = 15$ s. This is a reflection of the inward motion of the circular wave fronts that is expected when the apex of the inertial-wave cones approaches the HLS plane. To inspect that the motion of the circular wave fronts is inwards, the reader is referred to supplementary movie 8.

Figure 7 displays the azimuthal velocity u_θ for the associated images of figure 6. When comparing the panels in the left-hand column of figure 7 with those in the middle and right-hand columns, note the difference in the ranges over which the colourbars extend. The colourbar for the left-hand column shows $-0.01 \lesssim u_\phi/u_0 \lesssim 0.01$ while those of the middle and right-hand columns display $-0.1 \lesssim u_\phi/u_0 \lesssim 0.1$. Thus, the velocities in the

https://doi.org/10.1017/jfm.2026.11199 Published online by Cambridge University Press

panels in the left-hand column are an order of magnitude smaller than those of the middle and right-hand columns. Therefore, the panels in the left-hand column illustrate that there exists essentially no azimuthal velocity in the HLS plane. The large-scale red and blue patches visible in the panels of the left-hand column probably constitute experimental noise. That is, some very weak, random flow motion induced as the vortex ring travels across the HLS plane. When the panels of the left-hand column are plotted using the same colourbar range as used for the middle and right-hand columns its three panels are, essentially, uniformly white. The situation is different for the ring at $Ro = 4.77$ (2 rpm) in the middle column of plots in figure 6. The area to note is the circular, blue structure in the top two images. This area represents an area of anticyclonic swirling motion ahead of the vortex ring as it approaches the HLS plane. At $t = 15$ s, after the ring has passed the HLS plane, the centre portion of the image displays positive (red) velocities. These correspond to a cyclonic swirling motion of the liquid in the rear of the vortex rings. Note that the images in the left-hand and middle columns of figure 6 had not indicated any Coriolis effects on the radial flow component for $Ro = 4.77$. Thus, Coriolis forces affect the azimuthal component of the flow velocity somewhat more strongly than the radial component. For the ring that was subject to the strongest Coriolis effects, $Ro = 0.8$, in the right-hand column of images of figure 7 one can, once again, identify a clear signature of the inertial waves represented by a series concentric rings. These rings should move radially inwards, towards the centre as the vortex ring approaches the HLS plane from above ($t = 5$ s and $t = 7$ s) and radially outwards once it has passed the HLS plane ($t = 15$ s). Note that the ring-like structures in figures 6 and 7 are qualitatively similar to the structures in figures 4 and 5 of Messio *et al.* (2008) who investigated inertial waves generated by an oscillating disk in a rotating fluid.

The existence of the regions of anticyclonic and cyclonic swirling motion ahead and behind the vortex rings has already been commented on in Brend & Thomas (2009) based on the experiments using dye visualisation discussed in that paper. The anticyclonic motion ahead of the rings is induced by Coriolis forces acting on liquid transported radially away from the centre. Similarly, the cyclonic motion behind the ring arises when Coriolis forces act on the liquid being transported radially inward in that region of the flow field. Note that the cross product in the expression for the Coriolis force implies that, at any instant, the induced azimuthal flow results, in turn, in a secondary force component directed such that it opposes the radial motion of the fluid.

3.4. *Dispersion curves for the inertial waves*

3.4.1. *Data processing procedure to construct dispersion curve*

An approximate, rough experimental verification of (1.2) could, in principle, be obtained by manually measuring the angle θ between the axis of rotation and the direction of wave propagation from a sequence of images such as those shown in figures 4 and 5. However, it was decided to adopt more elaborate procedures.

Experimental data to confirm the dispersion relation of (1.2) were obtained by means of digital image-processing methodologies using custom Python routines developed as part of the data analysis. The process of finding the relationship between θ and particular frequencies filtered for, F_f, employed a two-point spatiotemporal correlation methodology relying on the frequency-filtered velocity fields $u'_H(p, q, t)$ of (3.2). The principle of the data-analysis approach applied is briefly illustrated and summarised with the aid of figure 8. Characteristic length scales in the p and q directions of the pixel array were obtained from the first zero crossing of the correlations. From these the angle θ follows from the trigonometric tangent ratio of both length scales.

https://doi.org/10.1017/jfm.2026.11199 Published online by Cambridge University Press

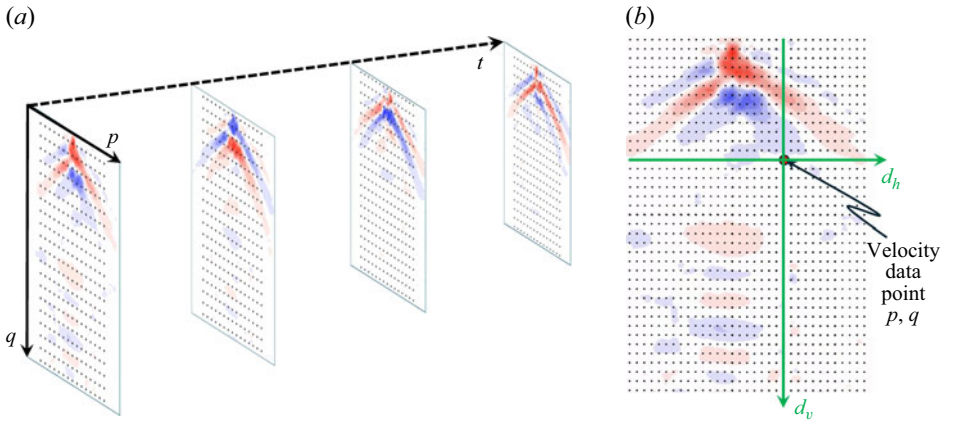


Figure 8. Schematic of data-point arrangement to aid data analysis. (*a*) Spatiotemporal grid. (*b*) Illustration of data-point distances d_h and d_v.

Each image consists of 149 × 239 velocity-data points, i.e. 149 rows of data points and 239 columns of data points. But, note that the camera was mounted sideways (portrait format) in the experiment to maximise the field of view in the x direction of figure 2(*b*). Therefore, rows of data points in figure 8 appear as columns, and columns appear as rows. Any particular data point p, q referred to is located at data row p and data column q with $p = 1 \ldots 149$ and $q = 1 \ldots 239$. For each experiment 3600 images were captured and each frame is associated with a time step t_i, with $i = 1 \ldots 3600$. The time associated with the 3600th frame is also referred to as $t_i = N_S$. In summary, the dataset for each frequency-filtered velocity field represents a three-dimensional array with $149 \times 239 \times 3600 \approx 12.8 \times 10^8$ entries.

The filtered velocity data $u'_H(p, q, t_i)$ for each particular data point p, q in figure 8(*b*) is compared with the corresponding velocity data for all other data points in its row and its column. This process is facilitated in terms of calculating correlations for velocity data of data-point pairs according to (3.3) and (3.4), where d_h and d_v represent the distance between a pair of data points in, respectively, the horizontal and vertical directions (see figure 8*b*):

$$r_h(p, q, d_h) = \int_0^{t_i = N_s} u'_H(p, q, t_i) \cdot u'_H(p + d_h, q, t_i)\, \mathrm{d}t_i, \tag{3.3}$$

$$r_v(p, q, d_v) = \int_0^{t_i = N_s} u'_H(p, q, t_i) \cdot u'_H(p, q + d_v, t_i)\, \mathrm{d}t_i. \tag{3.4}$$

However, in the context of the correlations, and with reference to the subsequent averaging of the correlations obtained, only the correlations for unique data-point pairs were calculated. The expression 'unique' is intended to mean that correlation results for multiply occurring data-point combinations only enter the averaging process once. Assume point (p, q), of row p, in figure 8(*b*) has already been compared with all points in the different columns of its row. A non-unique point pair will then occur while a point in a different column, γ, of row p is compared with the points in all other columns in that row and when the point in column γ is required to be paired with the point in column q. Redundant, non-unique data-point pairs were excluded using Python's *Itertools* library. The *Itertools* library provides functions for creating iterators for efficient looping within Python codes.

https://doi.org/10.1017/jfm.2026.11199 Published online by Cambridge University Press

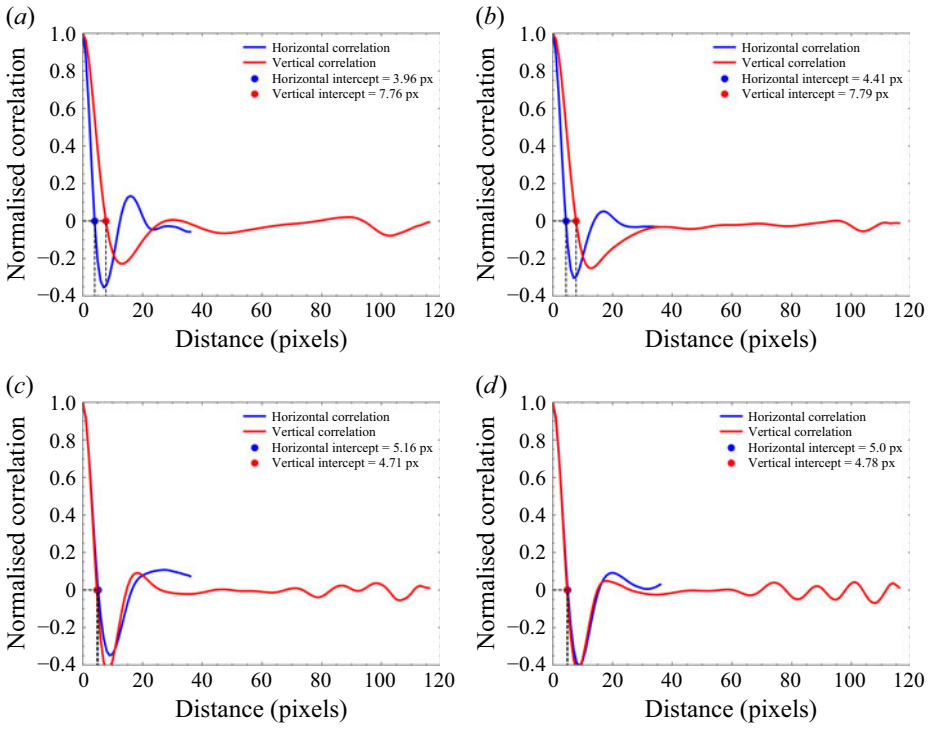


Figure 9. Averaged, normalised correlation data as a function of data-point distance for left and right sections of a vortex ring in the VLS plane at $Ro = 1.59$ (12 rpm): (*a*) 60° filter, left side; (*b*) 60° filter, right side; (*c*) 45° filter, left side; (*d*) 45° filter, right side. The decorrelation distances $D_{0,x}$ and $D_{0,y}$ are identified by the red and blue circular markers and the dashed lines superposed onto the curves displayed.

Once the correlations for all unique data-point pairs and all possible data-point distances in the vertical and horizontal directions have been calculated, the data for equal distances, in the vertical and horizontal directions, are averaged. That is, for instance, the correlations for all unique combinations of data-point pairs in the vertical direction that are separated by a distance of, say, ten data points are averaged to yield one mean value for that separation distance. A corresponding averaging is conducted for all other data-point separations in the vertical direction. The analogous process is then carried out for all possible separation distance in the horizontal direction. The mean values obtained in that way are then normalised by the mean value of the correlation coefficient obtained for autocorrelations at all data-point sites. That is, by correlations for the cases where $d_h = 0$ and $d_v = 0$. Sample data obtained by the process outlined above are displayed in figure 9. The results displayed in the figure are for a vortex ring at $Ro = 1.59$ and $Re = 10\,000$, where the original velocity field was filtered for frequencies corresponding to waves emitted at angles 60°(0.2 Hz) (figure 9*a*,*b*) and 45°(0.2828 Hz) (figure 9*c*,*d*). Note that our Python code was set up to separately process the data to the left and to the right of the axis of symmetry (axis of rotation). This approach was adopted to avoid the correlation reaching a secondary peak where the radial distance would reach across the axis of symmetry. Since a wave field is considered the value of the mean correlation data will oscillate between positive and negative values as one intersects across different phases. In an unbounded inviscid system, one would expect the oscillations to continue with constant amplitude. However, in a real fluid with viscous dissipation the magnitude of the oscillations will reduce, and this is reflected by the data in figure 9.

https://doi.org/10.1017/jfm.2026.11199 Published online by Cambridge University Press

From the data in figure 9 one obtains characteristic decorrelation distances. The characteristic decorrelation distance in the horizontal (D_h) and the vertical (D_v) direction is the distance at which the relevant correlation first adopts a value of zero. That is so, because a correlation coefficient of zero implies that the data are entirely uncorrelated. For waves this is the case when the phase difference is such that the data are shifted by half a wavelength. The values for the characteristic correlation distances for the left side and for the right side of the flow field are then averaged to yield final values. These distances, where the data are uncorrelated, are identified in figure 9 by the blue and red markers and the associated dashed lines. The angle of propagation for the wave mode considered then follows from simple geometry as

$$\theta = \tan^{-1}\left(\frac{D_v}{D_h}\right) . \tag{3.5}$$

Recall, from § 2, that data for 10 separate runs for constant values of the independent experimental parameters were performed and processed and the 10 values of θ for each particular frequency were then averaged. In that context also recall that each frequency-filtered velocity field represents a three-dimensional array with approximately 12.8×10^8 entries.

For the highest and lowest inertial-wave frequencies near, respectively, $\theta \approx 0°$ and $\theta \approx 90°$ (see figure 1) data are difficult to obtain. At $\theta = 0°$ and $\theta = 90°$ the expression (3.5) breaks down because the phases of the waves, identified by the blue and red lines in figure 1, are aligned with, respectively, the data-point columns and the data-point rows. That is, values for D_h and D_v do not exist. Moreover, near 90° one has $\cos\theta \approx 0$ such that ω is very small. Thus, only a very small number of wave phases can be captured and the correlation will not decrease sufficiently rapidly to accurately predict the wavelength. For these reasons the data analysis was restricted to frequencies with angles corresponding $10° \leq \theta \leq 80°$.

3.4.2. *Dispersion curves*

Figures 10 and 11 display the theoretical dispersion curve of (1.2) in comparison to experimental data processed by using the methodology outlined in § 3.4.1. The experimental data in figures 10 and 11 were obtained from a data analysis of the PIV data measured in the VLS plane of figure 2(*b*). Prior to applying the procedures of § 3.4.1 the velocity data for the VLS plane were separated into their axial and radial components. That is, into the velocity components in the direction of the x axis (axial component) and the y axis (radial component) displayed in figure 10. Both components were then analysed independently by applying the methodology of § 3.4.1. The results in figure 10 are based on the analysis of the data for the axial flow component while the data in figure 11 are based on the data for the radial component. The two figures display data for vortex rings at different values of the Rossby number to illustrate how the agreement between the theoretical dispersion curve and the experimental values improves as Coriolis effects become more dominant when the Rossby number decreases.

The graphs for both velocity components reveal a very good agreement between the theoretical and experimental data, across the expected frequency band, at the lowest Rossby number of $Ro = 1.59$. This represents a conclusive experimental confirmation of the emission of inertial waves. The agreement between the experimental data points and the theoretical curve deteriorates as the Rossby number increases, as one expects. According to (1.2), and supported by figure 3, the presence of inertial-wave structures diminishes as the background rotation rate Ω approaches zero. However, the deterioration

https://doi.org/10.1017/jfm.2026.11199 Published online by Cambridge University Press

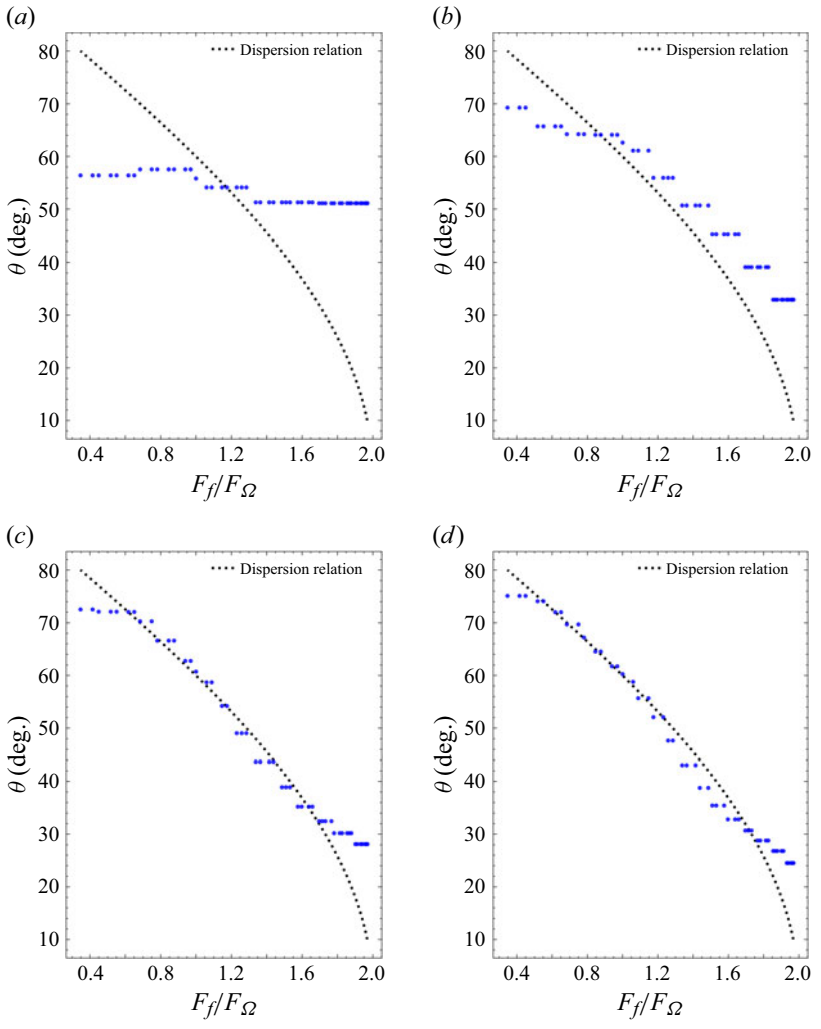


Figure 10. Measured inertial-wave frequencies θ (displayed as angles) as a function of the filter frequency, F_f, normalised by the rotation frequency of the turntable. F_Ω. The data are for (*a*) $Ro = 6.37$ (3 rpm), (*b*) $Ro = 3.18$ (6 rpm), (*c*) $Ro = 2.12$ (9 rpm) and (*d*) $Ro = 1.59$ (12 rpm). Here the axial flow field is used as the velocity being filtered.

of the agreement between experiment and theory is further augmented for conditions near $\Omega \approx 0$ because the number of frequency bins available for the Fourier analysis decreases, as was outlined in § 3.2.1. The issue regarding the number of frequency bins is particularly highlighted at the lowest rotation rate associated with $Ro = 6.37$, in figures 10(*a*) and 11(*a*), where all data points are grouped together in a very small number of bins for the angle θ.

3.5. *Distribution of the kinetic energy surrounding the vortex rings*

The inertial waves discussed in the preceding sections radiate energy away from the vortex rings. The PIV velocity data collected as part of the current study can be further analysed to obtain some first information relating to the process of the energy redistribution.

https://doi.org/10.1017/jfm.2026.11199 Published online by Cambridge University Press

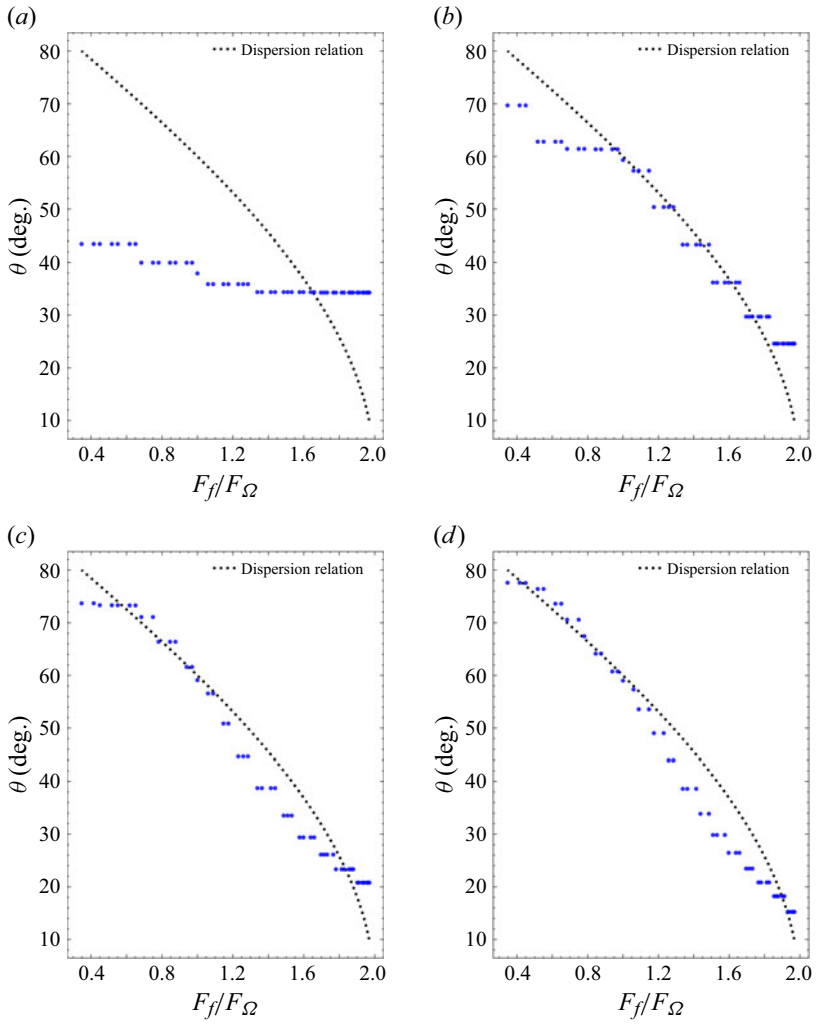


Figure 11. Measured inertial-wave frequencies θ (displayed as angles) as a function of the filter frequency, F_f, normalised by the rotation frequency of the turntable, F_Ω. The data are for (*a*) $Ro = 6.37$ (3 rpm), (*b*) $Ro = 3.18$ (6 rpm), (*c*) $Ro = 2.12$ (9 rpm) and (*d*) $Ro = 1.59$ (12 rpm). Here the radial flow field is used as the velocity being filtered.

The data in Brend & Thomas (2009) show that vortex rings produced by a nozzle–piston arrangement in a non-rotating fluid can be identified as coherent structures up to a distance from the exit nozzle of the order of 200 times the nozzle diameter. This implies that the kinetic energy associated with the rings remains located within a well-defined, propagating region of the flow field. However, as is also known from Brend & Thomas (2009) rings subject to background rotation disintegrate substantially earlier. This results in a lateral redistribution of the kinetic energy, and in rotating flow the process is further augmented by the energy that is fed into the inertial waves. Therefore, the available data from this study are now analysed to gain some first insight into how the available kinetic energy redistributes as the level of background rotation is successively increased.

The kinetic energy is based on velocity data captured in the VLS plane (see figure 2*b*). Contributions due to flow motion perpendicular to the VLS plane are therefore not

https://doi.org/10.1017/jfm.2026.11199 Published online by Cambridge University Press

accounted for. However, a comparison of figures 6(*b*) and 7 reveals that the radial and the azimuthal velocity are of the same magnitude. The necessity of neglecting the azimuthal energy contributions is a shortcoming associated with the two-dimensional PIV measurements. These do not allow for the monitoring of the temporal development of the azimuthal flow velocity in a coordinate system that would be required to travel with the vortex rings. Thus, the analysis and discussion to follow below are restricted to the energy contained in the $x-y$ plane of figure 2(*b*) only. The vertical light sheet has a total width of $2r_{max} = 690$ mm and it extends from the rotational axis at $r = 0$ to $r = r_{max}$ on both sides of the axis, such that the monitored region is $-1 \geq r/r_{max} \leq 1$. The flow field is divided into two sections. The central region is defined as $-0.33 \geq r/r_{max} \leq 0.33$, and the outer region as $r/r_{max} < -0.33$ and $r/r_{max} > 0.33$.

The PIV velocity data are associated with a rectangular grid of data points in the VLS data light-sheet plane in figure 2(*b*). The distance between each pair of data points within the grid is determined by the size of the PIV interrogation window selected within PIVlab as part of the data analysis. The height of the interrogation window in the vertical direction is referred to as h and its width in the radial direction is δr. Rotational symmetry of the PIV data around the x axis in figure 2(*b*) is assumed. Thus, each PIV data point is associated with a square-section toroid of fluid. The volume of each such toroid, with inner radius located at distance r from the rotational axis, is given by

$$V_{\delta r} = h \int_{r}^{r+\delta r} \int_{0}^{2\pi} r \, \mathrm{d}r \, \mathrm{d}\phi. \tag{3.6}$$

Thus, the further a toroid is away from the rotational axis the more volume is associated with it. Thus, the volume $V_{\delta r}$ can be interpreted as a dimensionless weighting factor. Therefore, the specific kinetic energy (energy/mass) for that torus, where the PIV velocity is $\boldsymbol{V}(r)$, is given by

$$\Delta E_{kin} = \frac{1}{2} V_{\delta r} \boldsymbol{V}^2(r). \tag{3.7}$$

Before calculating ΔE_{kin} of (3.7) for the toroid, the value of $V(r)$ of the right half of the velocity field and the corresponding value $V(-r)$ from the left half of the velocity field were averaged. The total specific kinetic energy is then given by a sum over all interrogation windows as

$$E_{kin} = \frac{1}{V_T} \sum_{IW} \Delta E_{kin}, \tag{3.8}$$

where the total volume V_T is the sum of all $V_{\delta r}$.

An example for the temporal development of the distribution of the kinetic energy is displayed in figure 12. For the data in the figure, time t was normalised by the length of the injection interval, $t_0 = 1$ s. The figure compares data for vortex rings at $Re = 10\,000$ for a non-rotating case ($Ro = \infty$), in figure 12(*a*), with the corresponding rotating equivalent at $Ro = 1.59$, in figure 12(*b*). Both figures show the total energy in the leftmost plot, the energy in the central region $r \leq 0.33 r_{max}$ as the middle plot and the energy in the outer region ($r > 0.33 r_{max}$) as the rightmost plot.

For the non-rotating case, figure 12(*a*) reveals that, as expected, the entire kinetic energy remains confined to the central region over the whole observation interval of 60 s. The kinetic energy reaches a peak of $E_{kin} \approx 0.025\ \mathrm{m^2\,s^{-2}}$ at $t/t_0 = 6.7$ after liquid injection commenced and then begins to gradually decrease.

The data for the corresponding ring developing subject to rotation, in figure 12(*b*), are markedly different. The energy in the central region displays its peak of $E_{kin} \approx$

https://doi.org/10.1017/jfm.2026.11199 Published online by Cambridge University Press

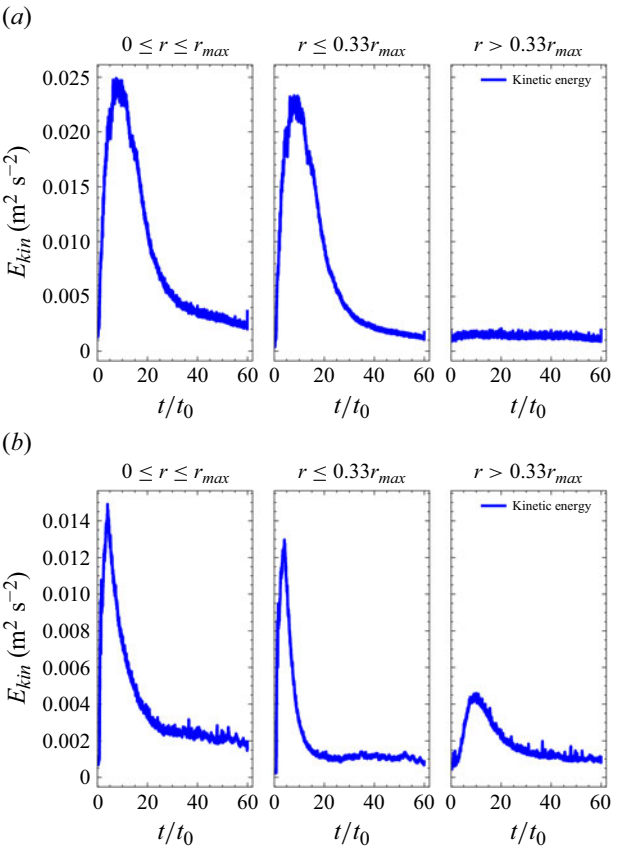


Figure 12. Kinetic energy (per unit mass) E_{kin} in the flow field as a function of time t normalised by the length of the injection interval, $t_0 = 1$ s. Data for ring ejection into (*a*) non-rotating liquid ($Ro = \infty$) and (*b*) rotating liquid at $Ro = 1.59$ (12 rpm). In each case the total kinetic energy is shown together with the fractions of the energy contained in the centre portion of the tank ($r \le 0.33r_{max}$) and in the off-centre region ($r > 0.33r_{max}$).

$0.013\,\mathrm{m^2\,s^{-2}}$ at $t/t_0 = 3.21$ with a subsequent energy decay. The energy peak in the rotating case can be seen to be narrower than that in the non-rotating case. That is because a fraction of the available energy is already being redistributed to the outer region of the flow field. The most prominent difference between the energy distribution in the non-rotating case in figure 12(*a*) and the rotating case in figure 12(*b*) is that there also appears an energy peak $E_{kin} \approx 0.005\,\mathrm{m^2\,s^{-2}}$ in the outer region, at $t/t_0 \approx 10$.

To quantify the energy redistribution further, the radial distance that contains 80 % of the kinetic energy within PIV image frames is investigated. To this end two equivalent integral sums of the kinetic energy are calculated across the flow field. One of the sums (r^+ limit) is evaluated by calculating the cumulative energy contribution by summing in the positive radial direction from $-r_{max}$ to $+r_{max}$ and the other one (r^- limit) in the negative direction. The purpose of calculating the two equivalent curves was to better highlight potential asymmetries in the left and right half of the VLS plane.

Figure 13 displays an example of the r^+- and r^--limit curves for a non-rotating case in comparison with a rotating case at $Ro = 1.59$. The data are for a vortex ring with $Re = 10\,000$ at an instant $t = 7.5$ s after the start of the ejection of water from the nozzle. The figure displays the cumulative energy, $E_{kin}(r)$, normalised by the total kinetic energy, $E_{kin_{max}}$, as a function the radial location, r, normalised by the nozzle diameter, r_0. The

https://doi.org/10.1017/jfm.2026.11199 Published online by Cambridge University Press

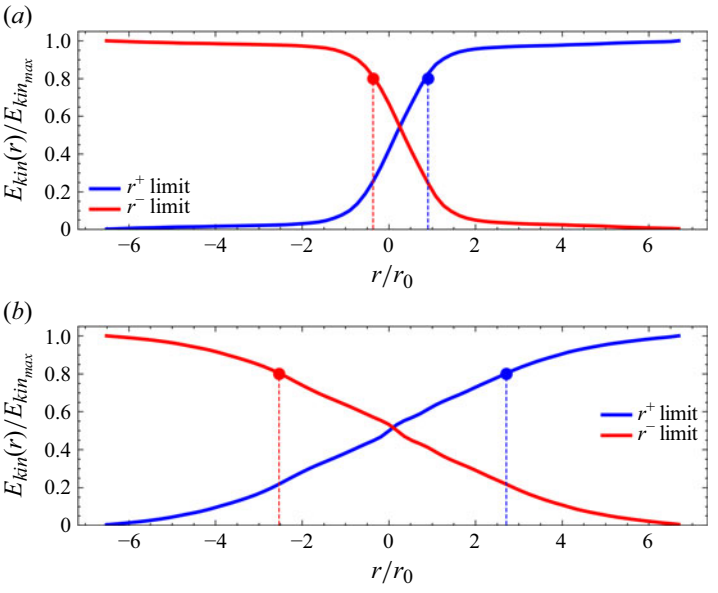


Figure 13. Normalised horizontal sum of kinetic energy for $Re = 10\,000$ at $t = 7.5$ s. Positive and negative radial thresholds are displayed separately: (*a*) $Ro = \infty$ (0 rpm) and (*b*) at $Ro = 1.59$ (12 rpm).

radial location of the 80 % limit is indicated by the dashed lines. It can be seen that the 80 %-limit region is substantially narrower for the non-rotating case in figure 13(*a*) than for the rotating case in figure 13(*b*). Figures 14(*a*) and 14(*b*) display the 80 %-limit intervals superposed onto the associated, unfiltered inertial-wave field for the data in figure 13. Note that one can identify the waves in figure 14(*b*) as unfiltered due to their structure of phases forming different opening angles θ relative to the axis of rotation. Figure 14 illustrates how the 80 %-limit interval for the non-rotating case in figure 14(*a*) narrowly encloses the vortex-ring structure whereas the corresponding limit for the rotating case in figure 14(*b*) essentially comprises inertial waves only.

Limit curves corresponding to those in figure 13 for the PIV image frame at $t = 7.5$ s were obtained for all frames of experimental runs at $Re = 10\,000$ to monitor the development of the width of the 80 %-limit interval as a function of time and of the Rossby number. The result is displayed in figure 15. The figure shows the mean radial position r/r_0 within which 80 % of the normalised kinetic energy is contained as a function of time t. For the non-rotating case ($Ro = \infty$) it can be seen that the energy remains confined within a radial location of $r/r_0 \approx 0.5$ until $t \approx 17$ s. The initially laminar ring then transitions to a turbulent state, upon which it loses its structural integrity resulting in a radial energy distribution. The data for $Ro = \infty$ in figure 15 adopt a maximum radial spread of $r/r_0 \approx 2$ at $t \approx 34$ s upon which viscous dissipation results in a gradual decay of the kinetic energy. A comparison of the data for the non-rotating case with the data for rotating cases at decreasing Rossby number reveals that increasing levels of rotation lead to a substantially increased radial energy transfer rate. For instance, for the highest level of rotation at $Ro = 1.56$ (12 rpm) the maximum of the 80 %-limit region is adopted at $t \approx 15$ s and extends to $r/r_0 \approx 4$. Corresponding to the non-rotating case, viscous dissipation then initiates a steady, slow decrease of the 80 %-limit region. Note that in the case of $Ro = 1.56$ a proper vortex ring essentially does not exist for extended time intervals. Figure 3 in Brend & Thomas (2009) shows that for Rossby numbers of the order of $Ro = 1.56$ the rings lose their structural integrity within a propagation distance of approximately 2−3 nozzle

https://doi.org/10.1017/jfm.2026.11199 Published online by Cambridge University Press

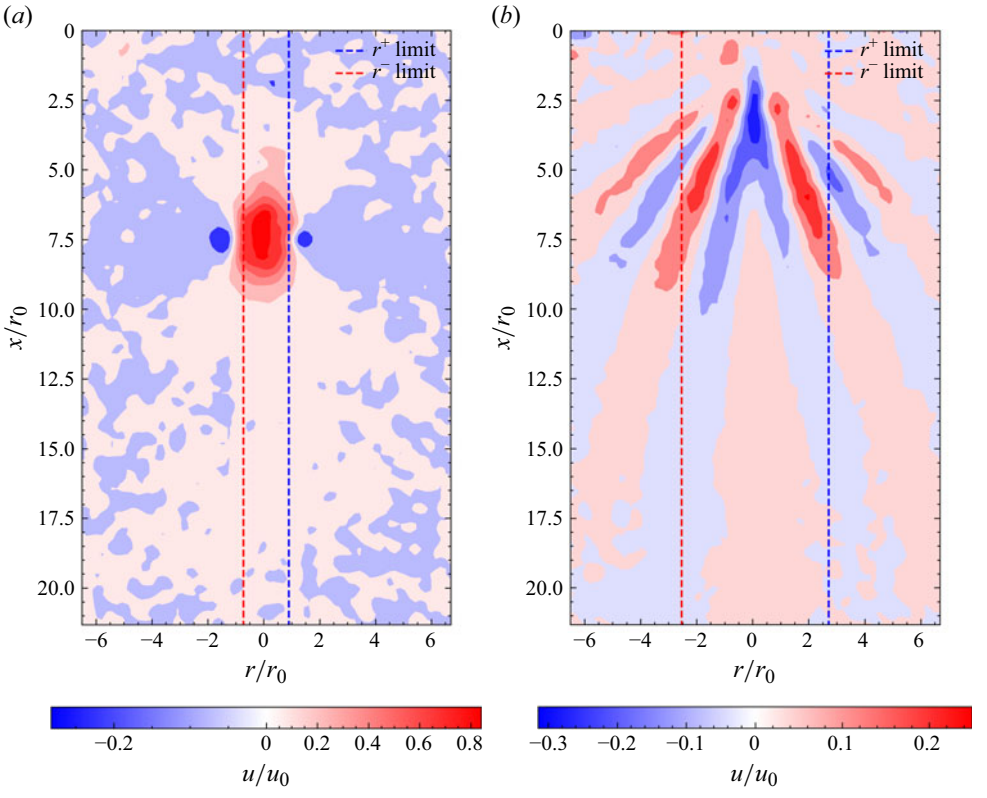


Figure 14. Visualisation of radial location of energy threshold for vortex rings with $Re = 10\,000$ at $t = 7.5$ s: (*a*) $Ro = \infty$ (0 rpm) and (*b*) at $Ro = 1.59$ (12 rpm).

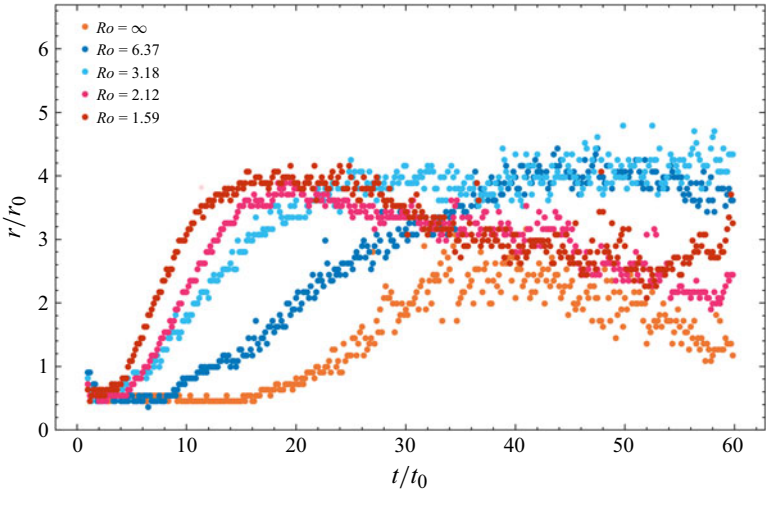


Figure 15. Mean radial position at which 80 % of the normalised kinetic energy is within r/r_0 against time for vortex rings with $Re = 10\,000$.

https://doi.org/10.1017/jfm.2026.11199 Published online by Cambridge University Press

diameters. Thus, and with reference to figure 14(*b*), the flow field essentially comprises a turbulent fluid region and inertial waves only. Therefore, a steady, slow decrease of the 80 % limit for r/r_0 can be observed that is akin to that for the non-rotating case ($Ro = \infty$). However, the cases at $Ro = 6.37$ and $Ro = 3.18$ in figure 15 do not display a narrowing of the 80 % limit within the observation window to $t = 60$ s. We speculate that this is due to the ring retaining its structural integrity for longer as the Rossby number increases while, at the same time, inertial waves are emitted. A final noteworthy observation from figure 15 is that for this particular series of experiments at $Re = 10\,000$ the 80 %-limit region does in no case exceed $r/r_0 \approx 4$. We presume that this upper limit may depend on the Reynolds number. However, that issue was not investigated as part of the current study.

4. Conclusion

The primary purpose of the experimental study summarised here was to verify the existence of an inertial-wave field associated with vortex rings translating along the axis of rotation through a rotating fluid. The existence of such a wave field has to be anticipated *a priori*. Its existence is also expected on the basis of the computational data for vortex rings in Verzicco *et al.* (1996), on the basis of the theoretical results of Taylor (1922) for the related cases of a sphere travelling through a rotating liquid along the axis of rotation, as well as on the basis of the computational results of Scase & Terry (2018) and Crowe *et al.* (2021) who investigated the corresponding motion for a Hill's spherical vortex.

However, there has hitherto not been an experimental confirmation of the existence of the inertial-wave field. The only existing experimental studies on vortex rings propagating through a rotating liquid along the axis of rotation are those by Verzicco *et al.* (1996) and Brend & Thomas (2009). The latter publication did not address the issue of inertial waves. Verzicco *et al.* (1996) did carry out PIV measurements that were conceptually very similar to those conducted as part of the current study. Nevertheless, their study was performed over 30 years ago. At the time the technological methodologies to collect and process the very large datasets as required to confirm the existence of the inertial-wave field by filtering velocity PIV data for individual wave modes and perform extensive correlations to obtain data for comparison with the theoretical dispersion curve of (1.2) were not yet available.

The main result of the current study is that these tasks, impossible at the time of the study by Verzicco *et al.* (1996), were successfully carried out to construct the dispersion relation (1.2) experimentally. In the context of the data analysis we visualised individual inertial-wave modes extracted from PIV velocity data collected in the VLS plane of figure 2(*b*). In particular, it was shown that it is possible to visualise the modes independently by analysing the u or the v velocity components in the VLS plane. Similarly, we visualised the inertial waves in the HLS plane of figure 2(*b*) by independently analysing the azimuthal and radial velocity components associated with the horizontal PIV light-sheet plane.

A quantitative comparison between the experimental data and the theoretical dispersion relation of (1.2) is displayed in figures 10 and 11. The comparison has revealed how the agreement between experiment and theory improves as the Rossby number decreases. A very good agreement between experiment and theory was found for low Rossby numbers when Coriolis effects dominate. The analysis has moreover shown that it is possible to independently construct the dispersion relation from the u- or the v-velocity component of the PIV data sampled in the VLS plane of figure 2(*b*).

The excitation of inertial waves naturally requires a redistribution of the energy that is injected into the flow field when the vortex rings are generated. Because of this, and

https://doi.org/10.1017/jfm.2026.11199 Published online by Cambridge University Press

because Verzicco *et al.* (1996) commented on the radiation of the energy, we briefly subjected the available PIV data to further analysis to obtain some first quantitative information as regards the energy redistribution associated with the formation of the inertial waves. It was found, as expected, that for vortex rings propagating in a non-rotating fluid the bulk of the energy stays confined to a region with a radial extension of the order of the nozzle diameter until the rings undergo laminar–turbulent transition. Thereupon, turbulent mixing results in a broadening of the region containing the bulk of the energy. However, in rotating flow and at low Rossby numbers where Coriolis forces dominate, the bulk of the energy quickly becomes distributed over a radial interval extending radially outwards as far as four nozzle diameters. The data collected that demonstrate this were, however, restricted to the case of Reynolds number $Re = 10\,000$ only. A potentially existing dependence of the energy redistribution process on the Reynolds number was not investigated as part of the current study.

Supplementary movies. Supplementary movies are available at https://doi.org/10.1017/jfm.2026.11199.

Declaration of interests. The authors report no conflict of interests.

References

Akhmetov, D.G. 2009 *Vortex Rings*. Springer Science & Business Media.

Brend, M.A. & Thomas, P.J. 2009 Decay of vortex rings in a rotating fluid. *Phys. Fluids* **21**, 044105.

Crowe, M.N., Kemp, C.J.D. & Johnson, E.R. 2021 The decay of Hill's vortex in a rotating fluid. *J. Fluid Mech.* **919**, A6.

Danaila, I., Kaplanski, F. & Sazhin, S.S. 2021 *Vortex Ring Models*. Springer.

Davidson, P.A. 2013 *Turbulence in Rotating, Stratified and Electrically Conducting Fluids*. Cambridge University Press.

Glezer, A. 1988 The formation of vortex rings. *Phys. Fluids* **31**, 3532–3542.

Helmholtz, H. 1858 Über Integrale der hydrodynamischen Gleichungen welche den Wirbelbewegungen entsprechen. *Crelle's J.* **55**, 25–55.

Jackson, O.C. 2025 An experimental study of the dynamics of vortex rings in a rotating fluid. PhD thesis, School of Engineering, University of Warwick, Coventry, UK. Available at: https://wrap.warwick.ac.uk/id/eprint/195731/.

Kaden, H. 1931 Aufwicklung einer Unstabilen Unstetigkeitsfläche. *Ing.-Arch.* **2**, 140–168.

Messio, L., Morize, C., Rabaud, M. & Moisy, F. 2008 Experimental observation using particle image velocimetry of inertial waves in a rotating fluid. *Exp. Fluids* **44**, 519–528.

Scase, M.M. & Terry, H.L. 2018 Spherical vortices in rotating fluids. *J. Fluid Mech.* **846**, R4.

Shariff, K. & Leonard, A. 1992 Vortex rings. *Annu. Rev. Fluid Mech.* **24**, 235–279.

Taylor, G.I. 1922 The motion of a sphere in a rotating fluid. *Proc. R. Soc. Lond. A* **102**, 180–189.

Thielicke, W. & Stamhuis, E.J. 2014 PIVlab - towards user friendly, affordable and accurate digital particle image velocimetry in MATLAB. *J. Open Res. Softw.* **2**, 30.

Thielicke, W. & Sonntag, R. 2021 Particle image velocimetry for MATLAB: accuracy and enhanced algorithms in PIVlab. *J. Open Res. Softw.* **9**, 12.

Verzicco, R., Orlandi, P., Eisenga, A.H.M., van Heijst, G.J.F. & Carnevale, G.F. 1996 Dynamics of a vortex ring in a rotating fluid. *J. Fluid Mech.* **317**, 215–239.

Widnall, S.E. & Sullivan, J. 1973 On the stability of vortex rings. *Proc. R. Soc. Lond. A* **332**, 335–353.

Widnall, S.E., Bliss, D.B. & Tsai, C.-Y. 1974 The instability of short waves on a vortex ring. *J. Fluid Mech.* **66**, 35–47.

Widnall, S.E. & Tsai, C.-Y. 1977 The instability of the thin vortex ring of constant vorticity. *Phil. Trans. R. Soc. Lond. A* **287**, 273–305.

https://doi.org/10.1017/jfm.2026.11199 Published online by Cambridge University Press